Interplay between theory and experiment in solid state inorganic chemistry†

Enric Canadell,*[a] Pablo Ordejón,[a] Emilio Artacho,[b] Daniel Sánchez-Portal,[c] Alberto García[d] and José M. Soler[b]

[a]Institut de Ciència de Materials de Barcelona (CSIC), Campus de la U.A.B., E-08193 Bellaterra, Spain. E-mail: canadell@icmab.es
[b]Departamento de Física de Materia Condensada, C-III, Universidad Autónoma de Madrid, 28049 Madrid, Spain
[c]Department of Physics and Materials Research Laboratory, University of Illinois at Urbana-Champaign, 61801 Illinois, USA
[d]Departamento de Física Aplicada II, Universidad del País Vasco, 48080 Bilbao, Spain

Recent advances in both first principles computational methodologies for complex systems and qualitative understanding of the electronic structure of solids now make a real dialogue between theoreticians and experimentalists possible. We discuss how this situation can lead to a fruitful interplay in inorganic solid state chemistry, considering selected examples, such as the structure of gold nanoclusters and nanowires, the absorption of atoms and molecules and growth of thin films on silicon surfaces, understanding the development of some structural modulations in low-dimensional transition metal oxides and bronzes, and the control of the transport properties of hybrid organic–inorganic charge transfer molecular solids.

Recent advances in density functional theory (DFT) methods[1,2] have made first principles calculations feasible for inorganic solids of practically any size. Besides the steady increase in computer power, the development of the so-called Car–Parrinello[3] and related methods,[4] order-N algorithms[5] and efficient pseudopotentials,[6] have been crucial in reaching this situation. Different DFT-based computational approaches are now available which have been shown to be both efficient and precise in performing atomistic simulations of many complex materials.[7–10] Of course, being able to calculate does not mean being able to understand in simple terms. And yet, this is an essential requirement for a fruitful collaboration between theoreticians and experimentalists. Of special note in the search for a simple yet rigorous conceptual framework by which to discuss the structure and properties of inorganic solids has been the approach pioneered by Hoffmann,[11] Burdett[12] and Whangbo,[13] which led to a series of ideas building a bridge between the concepts developed by solid state physicists and molecular chemists. We believe that it is not an overstatement to say that the almost simultaneous development of very efficient computational and conceptual tools has made (or can make) possible a real dialogue between theoreticians and experimentalists in solid state inorganic chemistry.

In this contribution we would like to discuss several problems which provide support for the previous statement. Just for the sake of convenience, we have chosen examples in which our groups have been involved; of course many other

contributions from other groups could equally have been chosen. The examples have been selected with a twofold purpose. Firstly, to point out how wide the spectrum of problems in which the interplay between theory and experiment is expected to be fruitful is, and secondly, to show that not every problem requires the same degree of computational accuracy. Simple methods still have a contribution to make in our search for a rational way to practice solid state inorganic chemistry. At the same time, the development of efficient and precise DFT methods has affirmed the belief that the longstanding psychological and practical barrier imposed by the size of many systems of practical interest is a thing of the past. The large-scale DFT calculations reviewed here were done using the linear scaling, numerical atomic orbitals DFT method implemented in the code SIESTA.[8] The simple tight binding calculations used an extended Hückel-type Hamiltonian.[14]

Gold nanowires and nanoclusters

The study of atomic nanostructures has experienced a considerable increase in interest over the last few years, mainly due to advances in preparation and characterisation techniques. Nanomanipulation at the atomic scale is opening the way to a whole new world of nanosize clusters and structures, with properties distinct from those of the macroscopic solids, and also of small molecules. The source of this difference in behaviour is precisely their nanometer scale, which is the critical size at which many properties start to change from molecular to solid-like. The case of metallic nanostructures is especially interesting because of the many useful potential applications (electric nanocontacts, catalysts, etc.), but also difficult from the theoretical point of view. In particular, nanoparticles of transition and noble metals present tremendous problems to theoreticians. The main reason is the relatively large number of atoms involved, but also the simultaneous presence of very compact d-orbitals (which yield very dense electronic distributions), and vacuum regions, which make the computations extremely demanding for the common implementations of first principles calculations for solid state systems (mainly based on plane waves). However, the role of the theory in the understanding of these systems is very important. The direct experimental measurement of their properties is often very difficult, or even impossible, and theory can provide answers to many of the questions that arise from

their study. For instance, the determination of the structure of these nanoaggregates is of paramount importance, since it greatly determines most of the rest of the properties, but is a difficult task from the experimental point of view. Here, the theory can guide the way, as we will illustrate in the following examples.

A recent spectacular achievement is the fabrication of monoatomic gold wires, which can be produced in several ways, for example, with the tip of a scanning tunnelling microscope (STM),[15] at mechanically controllable break junctions[16] or even with simple tabletop setups.[17] Several experiments on the transport properties of these nanowires (of gold and other metals) have been performed, showing quantization of the conductivity due to quantum confinement, which now seems to be quite well understood. Even more impressive is the possibility of visualizing these nanometer wires by means of transmission electron microscopy (TEM).[18] In these experiments, a bridge of four atoms connecting two gold tips was observed to be stable for more than two minutes. A striking fact about these observations was the spacing between atoms in the wire, which was 3.5–4.0 Å. Later reports[19] have increased this distance to about 5.0 Å, a value much larger than the typical Au–Au distance (ca. 2.5 Å in Au_2, and ca. 2.9 Å in bulk gold). In order to explain these unexpectedly large interatomic distances, several theoretical investigations have been carried out. A first study by Torres and co-workers[20] has shown that a linear gold chain (both infinite and finite) would break if the interatomic distances are larger than 3 Å, much smaller than the experimentally observed ones. This makes the experimental observations difficult to rationalize. However, in further work, Sánchez-Portal and co-workers[21] propose a mechanism for the observed interatomic distances in the nanowires. They showed that gold monoatomic wires exhibit a zigzag shape instead of a linear one if there is no tension in the chain. If the chains are tensioned, the zigzag geometry remains, with larger Au–Au–Au angles. Only under extreme tension do they become linear, although this occurs just before the breaking point. Fig. 1 shows the results of the calculations, where it can be clearly seen that, except for wire lengths close to the breaking limit, the ground state of the wire has a zigzag geometry. The reason for the chain taking a zigzag shape can be traced back to the metallic character of the gold atoms. The metallic character manifests itself in a tendency to increase the charge density by overlapping with neighbouring atoms in order to increase the binding energy. This makes the zigzag geometry more stable, since second neighbours come closer together. The structure does not collapse due to an increase of kinetic energy upon further closing of the angle, although, eventually, another more compact structure with lower energy can be obtained (corresponding to the drop in energy for small angles in Fig. 1). In order to understand the experimental observation of linear chains, and the very long interatomic distances observed, further calculations were done. It was shown that the barrier to rotation of the zigzag chain was very small: about 60 meV for a seven atom wire suspended between two pyramidal tips. At temperatures higher than 40 K, the rotation of the wire would be faster than the millisecond scale and, therefore, the TEM images would represent an average of the rotating wire. This provides a possible explanation for the observed interatomic distances: if the actual wires have an odd number of atoms, with those at the borders fixed by the contacts, the odd-numbered atoms would stay almost fixed on the same axis, while the even-numbered ones could rotate rapidly around the axis. The latter would then offer only a fuzzy image that could be missed by the TEM, while the fixed odd-numbered atoms would be clearly visible (as can be observed in Fig. 2). Therefore, the observed TEM interatomic distances would correspond to the distance between odd-numbered atoms in the zigzag chain, being thus much larger than the real interatomic distance between first neighbours. Further calculations of the vibrational frequencies were performed, as a possible way to experimentally verify the zigzag geometries.

Another case in which the experimental information has been only partial, and where theory has helped to uncover new information, is the study of gold nanoclusters. Among metallic nanoclusters, the case of gold is of special relevance, since new molecular nanocrystalline materials, considered as prototypes for electronic nanodevices and biosensors, have recently been synthesized using gold nanoclusters as building blocks.[22] Such advances in cluster growth and materials synthesis have motivated a number of theoretical and experimental studies on structural, dynamic, electronic, optical, and other physical and chemical properties of isolated and passivated gold clusters, as well as on the size dependence of these properties.[23,24] Structural characterization using X-ray powder diffraction (XRPD), high-resolution transmission electron microscopy (HRTEM), and scanning tunnelling microscopy (STM) has been attempted, but it is still very difficult to extract precise information on the structure of these systems from experimental data. Despite the existence of sophisticated experimental and theoretical tools, several structure-related issues remain unsolved. The main problem is the lack of a direct experimental technique to measure the structure of clusters.
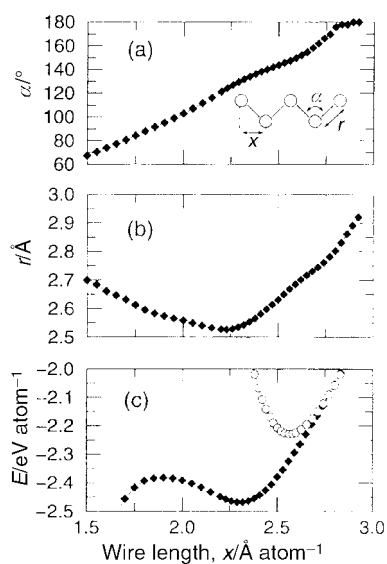
Fig. 1 First principles DFT results for the bond angle α (a) and bond length r (b) in a monoatomic gold wire with zigzag geometry, as a function of its length per atom. (c) Binding energy E in the zigzag (solid symbols) and linear wires (open symbols).
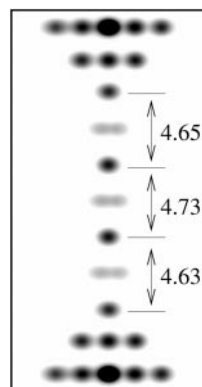
Fig. 2 Electron density (calculated from first principles) of a seven-atom wire suspended between two small pyramidal tips, averaged over all rotation angles around the wire axis, with a Boltzman factor at $T = 300$ K. The numbers are relaxed distances in Å.

The current approach is only able to infer the cluster structure from a comparison between experimental images (HRTEM, STM) or structure factors (XRPD) with those calculated from geometric models of clusters. Following this approach, a truncated decahedral motif was proposed as the most stable geometry for Au nanoclusters in the size range 1–2 nm. In recent work, several possible geometries were used to calculate the theoretical HRTEM images of gold nanoclusters.[25] Such images constitute a catalog to be used in a systematic comparison with the experimental results. In principle, the mentioned procedure should be sufficient to determine the cluster structures, since those methods have been successfully used for larger metal particles or bulk systems. However, in the case of Au clusters with sizes of 1–2 nm, the experimental resolution is not good enough to decompose the broad features in the XRPD structure factors and to obtain a conclusive determination of the structures.[24] Several theoretical calculations on the configurations of gold nanoclusters have been made using fixed cluster symmetries as constraints during a local optimization of the structure.[24] Nevertheless, a global, unconstrained optimization of the cluster structure is necessary for an exhaustive search of minima on the potential energy surface (PES).[26] Considerable efforts have been made recently towards this goal by Garzón and co-workers,[27,28] who have presented results on the most stable (lowest energy) configurations of intermediate-size (1–1.5 nm) Au_N ($N = 38$, 55, 75) nanoclusters, obtained through dynamic and evolutive (genetic/symbiotic) optimization methods.[29] The exhaustive search for minima was done using classical potentials (Gupta n-body potentials), but the most stable structures were further refined and analyzed by means of first principles DFT calculations. For the three sizes investigated, corresponding to the so-called magic number clusters, they did not obtain a single ordered structure with a definite symmetry as the global minimum. Instead, a set of several isomers nearly degenerate in energy was found. Moreover, most of these cluster configurations, including the lowest energy one, have little or no spatial symmetry, and a pair distribution function typical of glasses. Therefore, they can be classified as amorphous-like. The minimum energy structures for the three cluster sizes are shown in Fig. 3. These results, which were obtained for free clusters, were recently confirmed to hold also for aggregates passivated by a monolayer of thiol molecules, such as those used to produce nanocrystalline samples.

Control of the transport properties of molecular conductors through hydrogen bonding

Many of the interesting properties of low-dimensional metals are related to the special topology of their Fermi surface which, in the end, is imposed by the crystal structure. Thus, in order to discuss the origin of these properties and, more importantly, if we want to have some control over them, it is important to be able to understand how the shape of the Fermi surface is related to the crystal structure. This is very important, for instance, in low-dimensional molecular conductors, where there are many examples showing that very slight modifications in the crystal structure can drastically change the conducting properties.
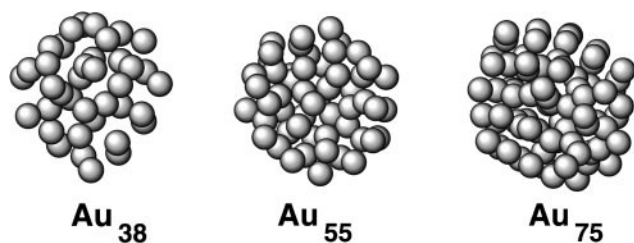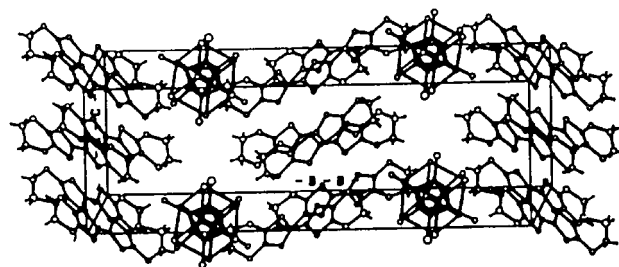

Fig. 4 Crystal structure of m-(BEDT-TTF)$_4$Re$_6$Se$_5$Cl$_9$·[DMF]. The DMF guest molecules are not shown.[31]

The situation is very different from that discussed in the previous section. The conductivity of a molecular metal is largely determined by the electrons near the Fermi level. Thus, in studying the transport properties of molecular metals, we need to focus on the partially filled bands of the system and the corresponding Fermi surface. Consequently, we do not need to use a theoretical approach that correctly describes all the filled levels of the system, i.e. the total energy, but just the partially filled levels. In other words, in understanding the transport properties of a molecular conductor, what we really need is to be able to estimate the interaction between the molecular level that is going to be partially filled (because of the electron transfer) and its nearest neighbours. This is something that is largely dictated by the corresponding overlap integrals, and very simple theoretical approaches, like the tight binding extended Hückel approach, have been of particular value in this area. In order to show how fruitful the collaboration between experimentalists and theoreticians in this field can be, we would like to discuss now a series of salts in which organic radical cations are associated with large all-inorganic anions leading to complex lattice architectures with metallic properties.[30] The goal of this collaboration was to explore some of the strategies that can be used when trying to tune in a rational way the transport properties of low-dimensional molecular conductors.

Let us consider the (BEDT-TTF)$_4$Re$_6$Se$_5$Cl$_9$·[guest] {BEDT-TTF = bis(ethylenedithio)tetrathiafulvalene, guest = DMF, THF, dioxane} series of salts[31] prepared by Batail and co-workers some years ago. The crystal structure of m-(BEDT-TTF)$_4$Re$_6$Se$_5$Cl$_9$·[DMF] is shown in Fig. 4, and consists of layers of BEDT-TTF donors alternating with layers of the [Re$_6$Se$_5$Cl$_9$]$^-$ cluster. As shown in Fig. 4, some empty space remains between the cluster anions. Solvent molecules (not shown in Fig. 4 for clarity) occupy these holes and give cohesion to the structure. It is important to realise that several of the hydrogen atoms of the BEDT-TTF donor point towards the solvent position and, thus, the donor layer and the solvent molecules are related through hydrogen bonds. Hence, the possibility of changing the internal structure of the donor layers (and, therefore, some of the transfer integrals of the donor sublattice) by appropriately replacing the solvent molecules immediately came to mind.

BEDT-TTF

DMF   THF   dioxane

Fig. 3 Most stable structures of three gold clusters, with 38, 55 and 75 atoms respectively, obtained from first principles DFT calculations.

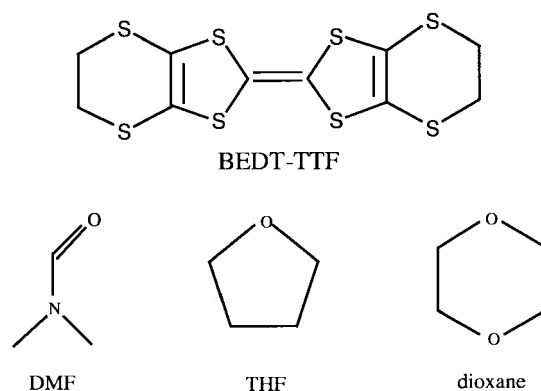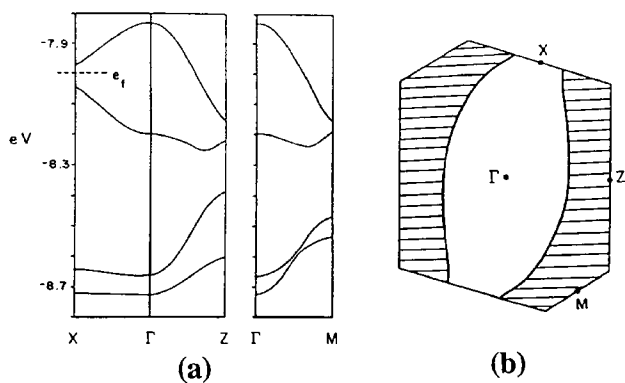**Fig. 5** Calculated band structure (a) and Fermi surface (b) for *m*-(BEDT-TTF)$_4$Re$_6$Se$_5$Cl$_9$·[DMF]. The dashed line in (a) indicates the Fermi level. Γ, X, Z and M refer to the wave vectors (0, 0), (a*/2, 0), (0, c*/2) and ($-a$*/2, c*/2), respectively. In (b), the wave vectors of the shaded and unshaded regions refer to filled and unfilled band levels, respectively.

Fig. 6 Fermi surface calculated for: (a) *t*-(BEDT-TTF)$_4$Re$_6$-Se$_5$Cl$_9$·[DMF] and (b) (BEDT-TTF)$_4$Re$_6$Se$_5$Cl$_9$·[dioxane]. The wave vectors of the shaded and unshaded regions refer to filled and unfilled band levels, respectively.

The calculated band structure near the Fermi level for the donor layers of *m*-(BEDT-TTF)$_4$Re$_6$Se$_5$Cl$_9$·[DMF] is shown in Fig. 5a. Since the unit cell of the donor layer contains four molecules, there are four bands mainly derived from the BEDT-TTF HOMO (highest occupied molecular orbital). With the average charge required by the stoichiometric formula, *i.e.* (BEDT-TTF)$^{+1/4}$, there are seven electrons to fill these bands. As shown in Fig. 5a, the Fermi level associated with this filling intersects the highest of the four bands only, which is, consequently, half-filled. The partially filled band is dispersive along both the a* (*i.e.* $\Gamma{\to}X$) and c* (*i.e.* $\Gamma{\to}Z$) directions. However, the dispersion along a* is smaller so that the Fermi level does not intersect the band along this direction, leading to the open Fermi surface shown in Fig. 5b. According to this result, *m*-(BEDT-TTF)$_4$Re$_6$Se$_5$Cl$_9$·[DMF] should be a pseudo-1D metal.

Interestingly, at the X point, the dispersion curve shows a minimum which lies very near the Fermi level (*ca.* 0.03 eV). A slight perturbation of the lattice affecting the transfer integrals could result in the Fermi level intersecting the band along the a* direction as well and, thus, leading to a closed 2D Fermi surface. Since in this process the X point becomes the locus of a van Hove singularity in the density of states, the physical properties of this type of material could be very exciting to study. The question was: how to induce these perturbations? With the structural information in mind, it was clear that by changing the nature of the guest molecules filling the cavities in between the clusters, slight displacements of the BEDT-TTF molecules would be induced through hydrogen bonding. Thus, for this particular lattice, it was quite apparent that there was the possibility of changing the electronic structure (and thus the transport properties) by using different types of solvent molecules.

Following this reasoning, four different salts of this type were prepared: *m*-(BEDT-TTF)$_4$Re$_6$Se$_5$Cl$_9$·[DMF], *t*-(BEDT-TTF)$_4$Re$_6$Se$_5$Cl$_9$·[DMF], (BEDT-TTF)$_4$Re$_6$Se$_5$Cl$_9$·[THF] and (BEDT-TTF)$_4$Re$_6$Se$_5$Cl$_9$·[dioxane].[31] Indeed, the internal structure of the donor slabs of these salts showed noticeable differences, although the main architecture was retained. The calculated Fermi surfaces for *t*-(BEDT-TTF)$_4$-Re$_6$Se$_5$Cl$_9$·[DMF] and (BEDT-TTF)$_4$Re$_6$Se$_5$Cl$_9$·[dioxane] are shown in Fig. 6a and b, respectively. While the Fermi surfaces of *m*-(BEDT-TTF)$_4$Re$_6$Se$_5$Cl$_9$·[DMF] (Fig. 5b) and (BEDT-TTF)$_4$Re$_6$Se$_5$Cl$_9$·[dioxane] (Fig. 6b) are open, that of *t*-(BEDT-TTF)$_4$Re$_6$Se$_5$Cl$_9$·[DMF] (Fig. 6a) is closed. Thus it is clear that, without disturbing the main architecture of the lattice, just by appropriately changing the nature of the guest molecules, the topology of the Fermi surface can be changed and, thus, the transport properties of the system can be modified.
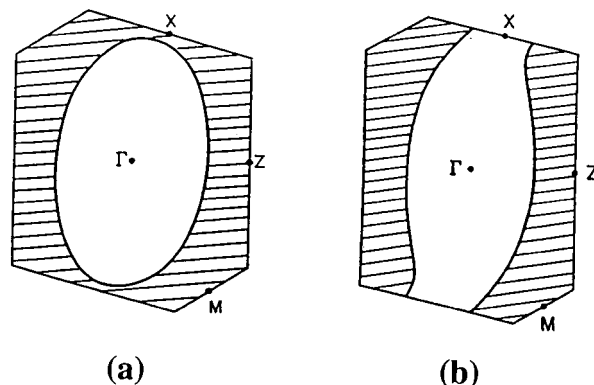
There is another aspect of the strategy outlined above which deserves comment. Depending on the nature and shape of the guest molecule, the size and hydrogen bonding requirements of the cavity can be fulfilled to a different extent. Thus, the guest molecule will have some degree of freedom within the cavity and this can lead to some disorder. For instance, it was the recognition of the inversion disorder of the solvent molecule in (BEDT-TTF)$_4$Re$_6$Se$_5$Cl$_9$·[THF] that prompted the choice of dioxane as a possible guest molecule in order to reduce such disorder. Indeed, (BEDT-TTF)$_4$Re$_6$Se$_5$Cl$_9$·[dioxane] has a highly ordered structure. Since it is well known that disorder can have a strong influence on the conductivity of molecular metals, this affords another strategy to slightly change the transport properties of this lattice. It is expected that when the degree of disorder decreases, the probability of electron localisation and, thus, activated conductivity, will also decrease.

The degree of disorder decreases from *m*-(BEDT-TTF)$_4$Re$_6$-Se$_5$Cl$_9$·[DMF], to (BEDT-TTF)$_4$Re$_6$Se$_5$Cl$_9$·[THF] and to (BEDT-TTF)$_4$Re$_6$Se$_5$Cl$_9$·[dioxane], something which is easily understandable in terms of the nature and shape of the different guest molecules. This is nicely reflected in the conductivity of these salts. All of them exhibit high room temperature conductivity and metallic behaviour. When the temperature is decreased, activated behaviour appears in a temperature range that decreases with the amount of disorder in the structure. A broad minimum in the resistivity curve is observed at *ca.* 90 K for *m*-(BEDT-TTF)$_4$Re$_6$Se$_5$Cl$_9$·[DMF], the most severely disordered material. It is shifted down to 50 K for (BEDT-TTF)$_4$Re$_6$Se$_5$Cl$_9$·[THF] and essentially vanishes in (BEDT-TTF)$_4$Re$_6$Se$_5$Cl$_9$·[dioxane].[31] In essence, changing the nature of the guest molecule allowed the suppression of the metal to insulator transition.

There is yet another possibility to modify the transport properties of this type of lattice. As shown by Batail and co-workers,[32] anions with practically the same shape but different charge can be prepared by changing the number of chalcogen and halogen atoms of the cluster. This immediately suggested the possibility of changing the number of electrons filling the HOMO bands of the donor lattice. This possibility has actually been realised and several salts with dianions, like Re$_6$S$_6$Cl$_8$$^{2-}$ or Re$_6$Se$_6$Cl$_8$$^{2-}$, have been prepared.[33] The donor lattices of these salts are very similar to those of the monoanions. Consequently, it is expected that the band structures will also be very similar and that the change in the transport properties will only be due to the different filling of the bands.

The calculated band structure and Fermi surface of the (BEDT-TTF)$_4$Re$_6$S$_6$Cl$_8$·[dioxane] salt are shown in Fig. 7.[34] The band structures of Fig. 7a and 5a are indeed very similar (the band structure of the (BEDT-TTF)$_4$Re$_6$Se$_5$Cl$_9$·[dioxane]

salt, although, of course, not identical, is in fact quite similar to that of Fig. 5a and, thus, it is not shown). Compare, for instance, lines $\Gamma \rightarrow X$ and $\Gamma \rightarrow Z$ in the two figures (note also that $\Gamma \rightarrow M$ in Fig. 5a corresponds to $\Gamma \rightarrow S$ in Fig. 7a). However, because of the smaller number of electrons filling these bands, the Fermi level now intersects two bands instead of just one. This leads to a Fermi surface for $(BEDT-TTF)_4Re_6S_6Cl_8 \cdot$ [dioxane] (Fig. 7b) which is very different in shape from that of $(BEDT-TTF)_4Re_6Se_5Cl_9 \cdot$[dioxane] (Fig. 6b).

In agreement with initial expectations, the physical behaviour of the two salts $(BEDT-TTF)_4Re_6S_6Cl_8 \cdot$[dioxane] and $(BEDT-TTF)_4Re_6Se_5Cl_9 \cdot$[dioxane] is very different. Both salts are metals at room temperature, but, while the latter keeps its metallic character down to very low temperatures, the former undergoes an abrupt metal to insulator transition at around 100 K, probably associated with a structural change. This transition can be suppressed under pressure.[34] The Fermi surface of Fig. 7b, which does not exhibit any apparent nesting, does not give hints about the origin of this transition. However, a careful analysis of the different transfer integrals and their geometry dependence suggests that a slight structural change can lead to a modified Fermi surface which is quite well nested by a vector with a c^* component of *ca.* 1/2.[34] This transition would thus be a structurally assisted Peierls distortion, as previously found for $(BEDT-TTF)_2ReO_4$.[35] In order to test this suggestion, diffuse X-ray scattering studies are needed. Again, the physical properties and Fermi surfaces of the dianion salt can be modified by changing the nature of the guest molecule. For instance, both $(BEDT-TTF)_4Re_6Se_6Cl_8 \cdot [H_2O]_2$ and $(BEDT-TTF)_4Re_6S_6Cl_8 \cdot [H_2O]_2$ are also room temperature metals and have donor lattices very similar to that of $(BEDT-TTF)_4Re_6S_6Cl_8 \cdot$[dioxane], but neither of them exhibits a metal to insulator transition like $(BEDT-TTF)_4Re_6S_6Cl_8 \cdot$ [dioxane].

It is clear that this type of salt offers fascinating possibilities for fine tuning of the transport properties. Carefully planned chemical changes c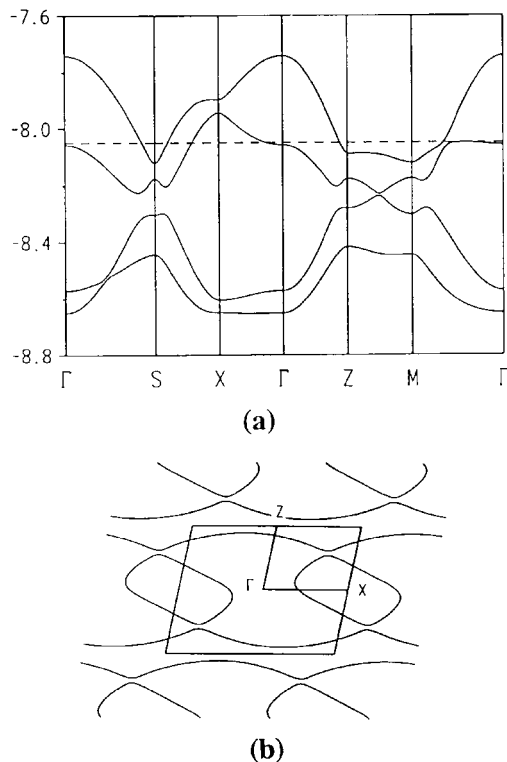an lead to modifications in: (a) the strength of some transfer integrals of the lattice, (b) the electron filling of the bands and (c) the degree of disorder. All of these changes have an important role in controlling the transport properties of this type of lattice but also those of other molecular metals. In recognising many of the ways in which this control can be effectively realised, a close collaboration between experimentalists and theoreticians has been very fruitful.

Understanding the structural modulations and resistivity anomalies of low-dimensional transition metal oxides and bronzes

Low-dimensional transition metal oxides and bronzes with partially filled t_{2g} bands have been the subject of many studies during the last decade.[13a,36–41] In particular, molybdenum oxides and bronzes have attracted the interest of the solid state community because of the physical properties they exhibit associated with their electronic instabilities. The blue bronzes $A_{0.3}MoO_3$ (A = K, Rb, Tl), the purple bronzes $A_{0.9}Mo_6O_{17}$ (A = Li, Na) and AMo_6O_{17} (A = K, Tl), as well as the Magnèli phases Mo_4O_{11}, Mo_8O_{23} and Mo_9O_{26} have been carefully studied.[13a,36–38] More recently, the large family of monophosphate tungsten bronzes has also received a lot of attention.[39–44] From the structural viewpoint, all these systems are 2D or 3D materials, but several of them behave as if they were 1D or pseudo-1D in terms of their physical behaviour.

The electronic instabilities of low-dimensional metals are related to the topology of their Fermi surface. When a piece of a Fermi surface can be translated by a vector q and superimposed on another piece of the Fermi surface, the Fermi surface is said to be nested by the vector q. An example of a perfectly nested Fermi surface is shown in Fig. 8. Metals with nested Fermi surfaces are susceptible towards a modulation with wave vector q of their charge or spin density, which destroys the nested portions of the Fermi surface. Thus, if the nesting is complete, like that in Fig. 8a and b, after the appearance of the modulation the entire Fermi surface is destroyed. The system exhibits a metal to insulator transition. If the nesting is only partial, part of the Fermi surface will remain after the appearance of the modulation and the transition will be of the metal to metal type. Metal to insulator transitions associated with such charge density or spin density waves are frequently observed at low temperature in 1D or pseudo-1D metals.[13] The potassium blue bronze is a typical example of a low-dimensional metal with a completely nested

(a)

(b)

Fig. 7 (a) Band structure and (b) Fermi surface for the donor layers of $(BEDT-TTF)_4Re_6S_6Cl_8 \cdot$[dioxane]. The dashed line in (a) indicates the Fermi level. Γ, X, Z, M and S refer to the wave vectors (0, 0), $(a^*/2, 0)$, $(0, c^*/2)$, $(a^*/2/, c^*/2)$ and $(-a^*/2, c^*/2)$, respectively.
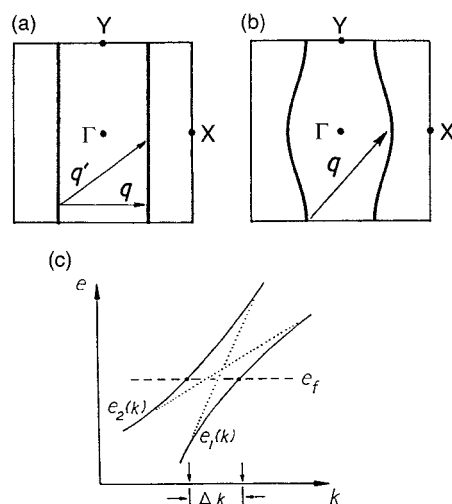

Fig. 8 Schematic representation of 1D (a) and a pseudo-1D (b) Fermi surfaces and the associated nesting vectors. (c) Schematic drawing of two band dispersion curves with an avoided crossing near the Fermi level.

Fermi surface which undergoes a metal to insulator transition associated with a charge density wave.[36,38]

Analysis of the Fermi surface nesting requires special consideration for a low-dimensional metal with several partially filled bands.[45] Fig. 8c illustrates two band dispersion curves with an avoided crossing in the vicinity of the Fermi level. With an increasing extent of band hybridisation, the separation Δk between the Fermi vectors becomes larger. In general, such avoided crossings in band dispersion surfaces lead to avoided crossings in the corresponding Fermi surfaces. Therefore, a low-dimensional metal with several partially filled bands may give rise to apparently unnested Fermi surfaces, although their intended surfaces (that is, those expected in the absence of the avoided crossings) are all nested. In such a case, the nesting is hidden by the avoided crossings. Such hidden, nested Fermi surfaces, can lead to charge density waves (CDWs), thereby destroying the nested portions of the combined Fermi surfaces. Thus, to understand the CDW phenomenon of a low-dimensional metal with several partially filled bands, it is essential to search for nesting in the intended, hidden Fermi surfaces.

The potassium purple bronze KMo_6O_{17} has separated Mo–O layers of composition Mo_6O_{17}, which are made up of both MoO_6 octahedra and MoO_4 tetrahedra (Fig. 9). The sodium and thallium purple bronzes are similar in structure to the potassium purple bronze. The potassium purple bronze is a 2D metal above 120 K, at which temperature it undergoes a CDW phase transition.[38,46–48] It remains 2D metallic after this phase transition. Diffuse X-ray scattering and electron diffraction studies show the occurrence of superlattice spots at $a*/2$, $b*/2$ and $(a*-b*)/2$ below 120 K.[48] According to the thermoelectric power measurements, the major carriers for electrical transport are electrons and holes above and below 120 K, respectively. Hall effect measurements show that both electrons and holes are present below 120 K. According to these observations, several partially filled d-block bands are present in KMo_6O_{17}. In electrical, CDW and other physical properties, the sodium and thallium purple bronzes are similar to KMo_6O_{17}.[47]

As shown in Fig. 9a, three different types of Mo atoms in AMo_6O_{17} exist.[49] According to both electronic band structure calculations[50] and a study of the bond-valence-sum analysis of the metal–oxygen bond lengths,[49] the d electrons of KMo_6O_{17} reside primarily in the MoO_6 octahedra of Mo(III). Consequently, the Mo_2O_9 layer formed by the inner two octahedral sublayers plays an important role in determining the electronic
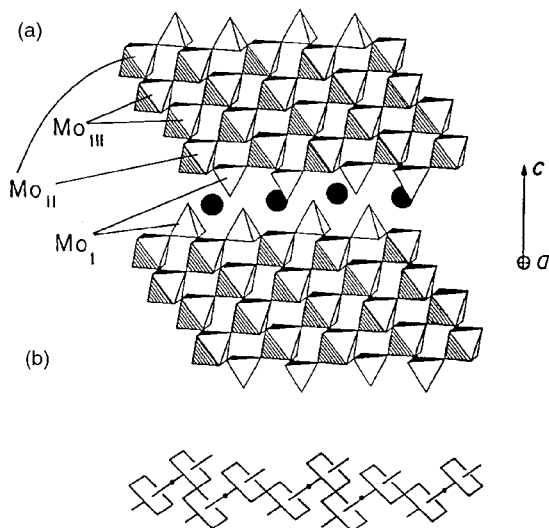
structure of KMo_6O_{17}. The Mo_2O_9 layer is shown schematically in Fig. 9b. A projection view of the Mo_2O_9 layer along the c-axis is given in Fig. 10a.

KMo_6O_{17} has three electrons per unit cell to fill its three lowest-lying d-block bands so that there are three partially filled d-block bands. The Fermi surfaces of the three bands are shown in Fig. 11a–c.[45] These surfaces are all 2D in nature, and their individual partial nesting does not explain the observed CDW vectors. The three surfaces are combined together in Fig. 11d which, upon neglecting the avoided crossings, can be decomposed into three sets of nested 1D surfaces, as illustrated in Fig. 11e. The 1D Fermi surfaces are perpendicular to the a, b and $(a+b)$ directions of the trigonal lattice.

To a first approximation, therefore, the three partially filled bands of KMo_6O_{17} are derived from three 1D bands dispersive along the a, b and $(a+b)$ directions. This conclusion is consistent with the structural and electronic properties of this bronze. As mentioned previously, the conducting electrons are confined to the inner Mo_2O_9 layers (see Fig. 9b and 10a). These layers can be constructed from Mo_2O_{10} zigzag chains, running along the a, b or $(a+b)$ directions, by sharing their axial oxygen atoms, as shown in Fig. 10b–d. The partially filled bands of KMo_6O_{17} are made up of the t_{2g}-orbitals of MoO_6 octahedra. As illustrated in Fig. 10e, the t_{2g}-orbitals are contained in the planes of the chains (that is, those defined by the equatorial oxygen atoms) running along the a, b and $(a+b)$ directions. Thus, the t_{2g}-orbitals are p-orbitals along the intrachain directions, but d-orbitals along the interchain directions. Consequently, the band associated with each of the t_{2g}-orbitals is dispersive along the associated intrachain direction, but dispersionless along the associated interchain direction. In addition, due to the local orthogonality of the t_{2g}-orbitals, the
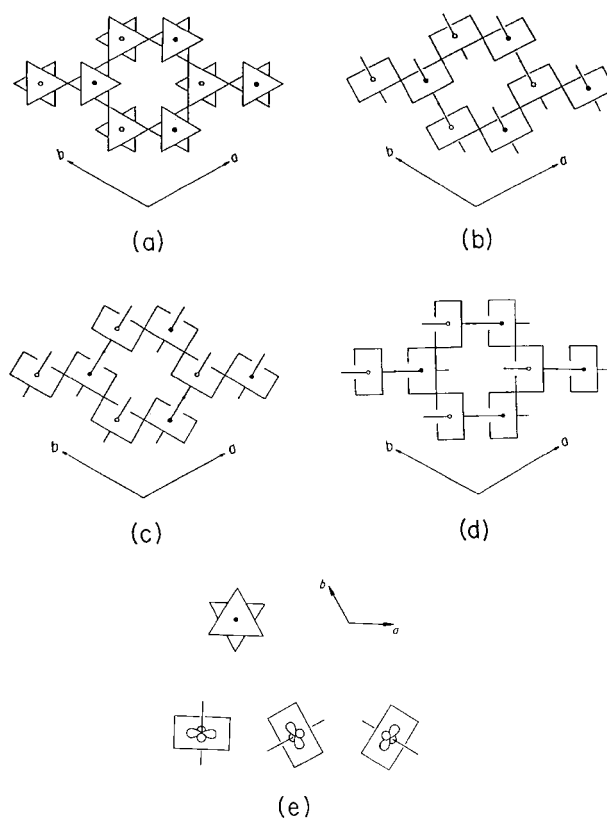

(a)　　　　　　　　(b)

(c)　　　　　　　　(d)

(e)

Fig. 10 Schematic view of the Mo_2O_9 trigonal layer present in the purple bronze KMo_6O_{17}. The projection view perpendicular to the layer is shown in (a). The Mo_2O_9 layer is constructed in terms of the Mo_2O_{10} zigzag chains running along the a, b and $(a+b)$ directions in (b), (c) and (d), respectively. Perspective views of the three t_{2g}-orbitals of an MoO_6 octahedron in the Mo_2O_9 layer are shown in (e), where the d-orbital containing planes are aligned along the a, b and $(a+b)$ directions of the Mo_2O_9 layer.

(a)

(b)

Fig. 9 (a) Perspective view of two adjacent Mo_6O_{17} layers of KMo_6O_{17}. The c-axis is perpendicular to the layer and the a-axis is perpendicular to the plane of the drawing. (b) Schematic view of the inner Mo_2O_9 layer in KMo_6O_{17}.
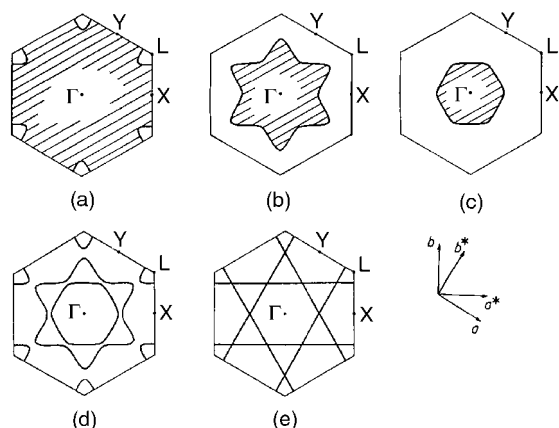
Fig. 11 Hidden nesting in the purple bronze KMo_6O_{17}. The calculated Fermi surfaces for the three partially filled d-block bands are shown in (a), (b) and (c), the combined Fermi surfaces in (d), and the hidden 1D Fermi surfaces in (e).

Fig. 12 Schematic representation of the X-ray pattern in the (a^*, b^*) plane above 120 K expected from the hidden nesting of KMo_6O_{17}. The heavy dots refer to Bragg reflections.

three chain bands resulting from the t_{2g}-orbitals are practically independent of one another, to a first approximation.[13a,45,50] Thus, for qualitative purposes, the bottom three d-block bands of KMo_6O_{17} can be approximated by the three independent 1D bands resulting from the t_{2g}-orbitals of each octahedra. It is these three 'hidden 1D bands' that are responsible for the hidden nesting shown in Fig. 11e.[45]

The electronic structure of KMo_6O_{17} is essentially represented by the three hidden 1D bands. Since there are three electrons to fill these bands, each band is half-filled. Consequently, the t_{2g}-block bands of KMo_6O_{17} can be viewed as a superposition of three almost independent half-filled 1D bands. It is this observation that led to the formulation of the concept of hidden nesting.[45]

A CDW formation introduces an additional periodicity of electron density distribution into the lattice and, hence, gives rise to superlattice reflections in the X-ray or electron diffraction pattern below the CDW phase transition temperature T_p. At temperatures above T_p, a nested 1D Fermi surface leads to CDW fluctuations. The latter cause planar diffuse scattering and, hence, $2k_f$ diffuse lines between layers of main Bragg reflections in X-ray diffraction patterns.[48,51] Thus, like any 1D metallic system with CDW instability, KMo_6O_{17} was predicted[45] to show 1D CDW fluctuations above 120 K and, hence, diffuse lines in the X-ray patterns. As schematically shown in Fig. 12, the diffuse lines resulting from the CDW fluctuations of the chains along the a, b or $(a+b)$ directions should be perpendicular to the chain direction and are located at the midpoints between the rows of the main Bragg spots perpendicular to the chain direction. Thus, the three sets of the diffuse lines should form hexagons around each main Bragg reflection spot (Fig. 12).

The pattern of diffuse lines predicted by Fig. 12 was observed by diffuse X-ray scattering experiments on AMo_6O_{17} (A = K, Na) at room temperature.[45] As the temperature is lowered below 120 K, the diffuse lines in Fig. 12 condense into satellite reflections at $a^*/2$, $b^*/2$ and $(a^*-b^*)/2$, which are the cross-section points of the diffuse lines. The nesting in the real Fermi surfaces (Fig. 11d) is not as complete as in the hidden surfaces (Fig. 11e), so that some small pieces of the Fermi surface (for example, small electron and hole pockets) may remain (especially in the avoided crossing regions) after the CDW phase transition. This would explain the semimetallic properties of AMo_6O_{17} observed below 120 K by galvanometric measurements.[38,46] Angle-resolved photoemission experiments on the sodium purple bronze also confirmed the occurrence of hidden nesting in these bronzes.[52,53]

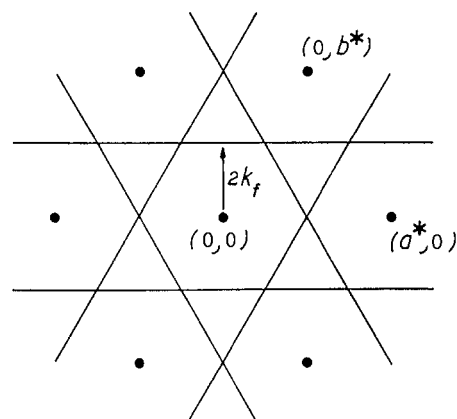The concept of hidden nesting was soon found to be essential in explaining the resistivity anomalies of a number of oxides and bronzes, like the Magnéli phases γ- and η-Mo_4O_{11}[54] and the family of monophosphate tungsten bronzes $(PO_2)_4(WO_3)_p(WO_3)_q$ (p and q are integer numbers related to the width of the octahedral layers).[44] These solids also contain metal–oxygen layers made up of MO_6 octahedra and possess partially filled t_{2g}-block bands. As for the purple bronzes, the three t_{2g}-block orbitals of each MO_6 octahedron are contained in three mutually orthogonal planes, and act as δ-orbitals toward the M–O axes perpendicular to these planes. Consequently, as a first approximation, these metal–oxygen layers can be regarded as made up of three noninteracting sets of t_{2g}-orbital containing chains, as far as their t_{2g}-block bands are concerned. The interest of the Magnéli phases and the monophosphate tungsten bronzes is that the three t_{2g}-orbital containing chains are not equivalent.[43] This leads to interesting new features in the low temperature behaviour of these solids that have recently received a lot of attention.[36,39–43] Again, the understanding of the puzzling behaviour of these low-dimensional materials through the development of the hidden nesting concept was only possible because of close collaboration between theoreticians and experimentalists.

Absorption of atoms and molecules and growth of thin films on silicon surfaces

The field of deposition on surfaces is of great importance, especially in the case of silicon: most of the devices used in microelectronics are obtained by surface-related processes on the silicon substrate. Therefore, the possibility of growing new materials on silicon can open routes to applications in microelectronics devices, which makes the field of deposition and growth on silicon a very active one. Here theory has also contributed a large amount, together with experiment. We will discuss a few cases here as an illustration.

In recent years, it has become possible to grow epitaxial thin films of perovskite oxides on silicon. The importance of this is enormous: these oxides present a range of properties like ferroelectricity, high dielectric constant, high temperature superconductivity and giant magnetoresistance, to mention just a few. Thin films of $SrTiO_3$ (a material of high dielectric constant) and $BaTiO_3$ (a ferroelectric material) were recently[55] grown epitaxially on Si(001), opening the possibility for their use in integrated circuits, for instance as gate oxides for field effect transistors, or as storage media for non-volatile memories. The growth process is complicated and it seems that an essential step is the deposition of a sub-monolayer of Sr or Ba to avoid interdiffusion. Wang and co-workers[56] have studied the first stages of Ba deposition on a clean Si(001) surface, to understand the microscopic details of the growth process from its initial stages. The theoretical results are

complemented by experimental STM images, which give an idea of the most likely positions of the Ba atoms, and the evolution with Ba concentration of the surface. The theoretical calculations in the limit of low Ba concentration show that the most favourable site of absorption is the trench between rows of silicon dimers (site A in Fig. 13). This is in contrast with the situation found in other alkali and alkaline earth metals on silicon, where other sites (like the middle of a dimer, or the position between dimers) are the most stable. In the case of Ba (and also Sr), the large size of the metal atoms makes it possible to form four bonds with the four silicon atoms located at the dimer rows adjacent to site A, and this makes the site a very stable one (since the Ba atom bonds to the dangling bonds of the Si atoms). Site B is also relatively stable, but 0.8 eV higher in energy than A (since the bond is not directed towards the dangling bonds of the Si atoms). An analysis of the Mulliken populations and the transfer of charge at the A site shows that, despite the large difference in electronegativity between Si and Ba, which would suggest an ionic bond, the charge transfer is rather small (only 0.15 e). There is, however, a large redistribution of charge in the close surroundings of the Ba atom (from the 6s-orbitals to the 6p and 5d-orbitals). This suggests the formation of a covalent bond between the Ba atom and the surface, and explains the core-level shift experiments of Cheng and co-workers,[57] who found a small or zero charge transfer at low coverage, in contrast to the ionic character of the metal silicides obtained at high coverage (above 1 monolayer). The results of the calculation are also consistent with the STM experiments[58] which also indicate a small charge transfer from Ba to Si in the low coverage regime.

An interesting issue that remains to be solved is the observation of absorption sites by STM[58] which are not consistent with the theoretical results of the absorption energy presented above. Although most of the experimentally observed absorption sites correspond to the theoretically predicted minimum energy configuration (site A), some Ba atoms are absorbed above the mid-point of a Si–Si dimer. This corresponds to an energy maximum, according to the calculations, and therefore should be a very unlikely absorption site. Work in progress by Tobías and Ordejón[59] explains this contradictory result by suggesting that the Ba atoms observed at these sites are not on top of a dimer, but on a missing-dimer defect site. Since the Ba is a large atom, the STM image can not determine if the dimer is present or missing, so the experiment alone can not define the situation. The calculations indicate that the absorption of a Ba atom on top of a missing dimer is very favourable energetically (even more stable than the site A absorption), and therefore we should expect to observe some Ba atoms in these sites, which often occur on clean Si(001) surfaces.

A last illustration of the interplay between theory and experiment in surface problems is the recent observation of molecular orbital (MO) features in C_{60} fullerene molecules absorbed on Si(111) surfaces.[60] MOs represent such a cornerstone in our understanding of molecular bonding and structure that drawings of them can be found in any quantum chemistry book. However, direct experimental visualization has proven very difficult because of technical and conceptual problems (energy resolution, interaction with the substrate, etc). Recently, Pascual and co-workers[60] have reported the observation of clear MOs of C_{60} by means of STM imaging. The molecules were deposited on a Si(111) (7×7) surface, in which the fullerenes are firmly anchored (because of the dangling bonds in the clean surface, which bond to the C atoms of the fullerene). In the STM images, molecules with two different apparent sizes can be observed. Upon annealing at 600 °C, the 'large' molecules evolve into 'small' ones, indicating that the last case corresponds to a more stable absorbed configuration. For this configuration, a rich variety of internal structures can be observed in the experimental STM images. Fig. 14a–d shows some of the most characteristic shapes, which are reproducible under different experimental conditions. The molecules in Fig. 14a–c give evidence of the expected decrease of the icosahedral symmetry after interaction with the surface, since each one appears with an intramolecular pattern resembling the 3, 2 and 5-fold rotational symmetry of the free molecules, respectively.

The interpretation and explanation of the observed images is greatly facilitated by theoretical calculations. A detailed theoretical calculation of a STM image is a difficult and demanding task, since the interaction of the substrate, molecule and tip must be included. However, the clear intramolecular features of the observed C_{60} images suggest that some information can be extracted from a calculation of the MOs of the isolated molecule, as a first approximation to the experimental setup. To break the energy level degeneracies, and simulate the observed decrease of the molecular symmetry induced by the substrate, we applied a small strain along different molecular axes in the calculations. In doing so, we found that the experimental patterns are reproduced in great detail in the calculated shape of the new HOMO of this free but compressed molecule (Fig. 14e–g). Note that the HOMO level is the one that is expected to contribute to the STM current, and therefore its shape will be sampled in the STM image. Other combinations of MOs other than the HOMO give a substantially poorer comparison with the experimental images. The close agreement between theory and experiment reveals that only one of the MOs arising from the initially quintuply degenerate HOMO is mainly responsible for electron transport through the molecule. We note that, despite the strong interaction between molecule and surface, it is possible to
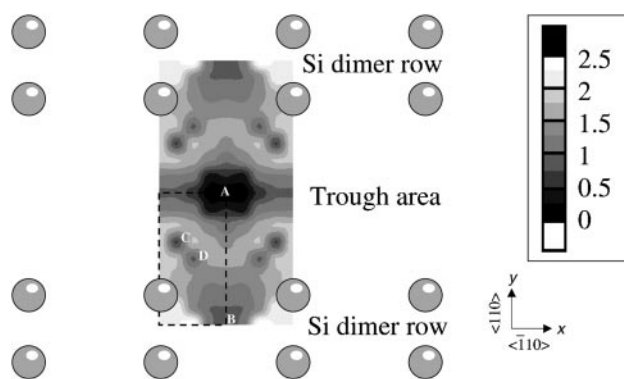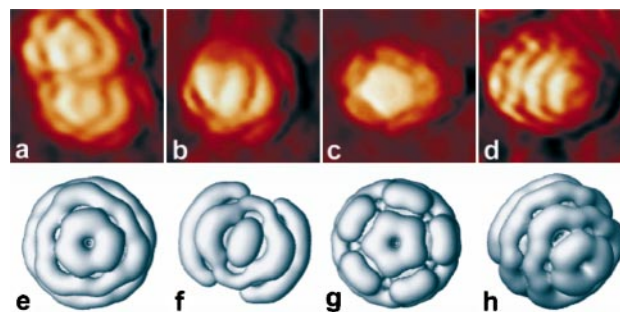

Fig. 13 Surface potential energy map (in eV) of a Ba atom on a Si(001) surface, from first principles DFT calculations. A sketch of the dimer rows in the (2 × 1) reconstruction is shown as a reference to the energy map.

Fig. 14 Comparison of the experimental STM images of individual C_{60} molecules on Si(111) (a–d) with the calculated molecular orbitals of the free molecule (e–h). In the calculation, a uniaxial deformation of 5% was applied along an axis of three- (e), two- (f), five- (g) and threefold symmetry (h). In (e–g), the axis was perpendicular to the plotting plane, whereas (h) was rotated an angle of 30°. In all cases, the orbitals plotted are the HOMO.

find experimental systems where a simple analysis in terms of MOs is justified, and highlights again the importance of the interplay between theory and experiment in extracting relevant physical and chemical information on the behaviour of solid state systems.

Concluding remarks

The development in recent years of very powerful DFT techniques has made it possible to perform reliable atomistic simulations of very complex materials. Almost simultaneously, a conceptual framework merging the approaches of solid state physicists and molecular chemists in order to understand the structure and properties of inorganic solids has also been put forward. As we have tried to make clear through the discussion of a few selected examples, these two developments now make possible a real and fruitful interaction between experimentalists and theoreticians on most aspects of contemporary solid state inorganic chemistry.

Acknowledgements

References

1 P. Hohenberg and W. Kohn, *Phys. Rev.*, 1964, **135**, 864.
2 W. Kohn and L. J. Sham, *Phys. Rev.*, 1965, **140**, 1133.
3 R. Car and M. Parrinello, *Phys. Rev. Lett.*, 1985, **55**, 2471.
4 M. C. Payne, M. P. Teter, D. C. Allan, T. A. Arias and J. D. Joannopoulos, *Rev. Mod. Phys.*, 1992, **64**, 1045.
5 For reviews, see: P. Ordejón, *Comput. Mater. Sci.*, 1998, **12**, 157; S. Goedecker, *Rev. Mod. Phys.*, 1999, **71**, 1085.
6 For reviews, see: W. E. Pickett, *Comput. Phys. Rep.*, 1989, **9**, 115; D. J. Singh, *Planewaves, Pseudopotentials and the LAPW Method*, Kluwer, Dordrecht, 1994; M. Fuchs and M. Scheffler, *Comput. Phys. Commun.*, 1999, **119**, 67.
7 M. Parrinello, *Solid State Commun.*, 1997, **102**, 107.
8 P. Ordejón, E. Artacho and J. M. Soler, *Phys. Rev. B*, 1996, **53**, R10441; D. Sánchez-Portal, P. Ordejón, E. Artacho and J. M. Soler, *Int. J. Quantum Chem.*, 1997, **65**, 453; E. Artacho, D. Sánchez-Portal, P. Ordejón, A. García and J. M. Soler, *Phys. Status Solidi B*, 1999, **215**, 809; P. Ordejón, *Phys. Status Solidi B*, 2000, **217**, 335.
9 P. E. Blöchl, *Phys. Rev. B*, 1994, **50**, 17953.
10 M. Bockstedte, A. Kley, J. Neugebauer and M. Scheffler, *Comput. Phys. Commun.*, 1997, **107**, 187.
11 R. Hoffmann, *Solids and Surfaces*, VCH, New York, 1988; R. Hoffmann, *Angew. Chem., Int. Ed. Engl.*, 1987, **26**, 846; R. Hoffmann, *Rev. Mod. Phys.*, 1988, **60**, 601.
12 J. K. Burdett, *Chemical Bonding in Solids*, Oxford University Press, New York, 1995; J. K. Burdett, *Prog. Solid State Chem.*, 1984, **15**, 173.
13 (*a*) E. Canadell and M.-H. Whangbo, *Chem. Rev.*, 1991, **91**, 965; (*b*) M. H. Whangbo, in *Crystal Chemistry and Properties of Materials with Quasi-One-Dimensional Structures*, ed. J. Rouxel, Reidel, Dordrecht, 1986, p. 27.
14 M.-H. Whangbo and R. Hoffmann, *J. Am. Chem. Soc.*, 1978, **100**, 6093; a modified Wolfsberg–Helmholtz formula was used to calculate the non-diagonal H_{ij} matrix elements (J. Ammeter, H.-B. Bürgi, J. Thibeault and R. Hoffmann, *J. Am. Chem. Soc.*, 1978, **100**, 3686).
15 N. Agraït, G. Rubio and S. Vieira, *Phys. Rev. Lett.*, 1995, **74**, 3995; J. I. Pascual, J. Méndez, J. Gómez-Herrero, A. M. Baró,

N. García, U. Landman, W. D. Luedtke, E. N. Bogachek and H. P. Cheng, *Science*, 1995, **267**, 1793.
16 C. J. Muller, J. M.. van Ruitenbeek and L. J. de Jongh, *Phys. Rev. Lett.*, 1992, **69**, 140; J. M. Krans, J. M. van Ruitenbeck, V. V. Fisun, I. K. Janson and L. J. de Jongh, *Nature*, 1995, **375**, 767; N. Agraït, J. C. Cuevas, A. L. Yeyati, B. Ludolph, A. Martín-Rodero, G. Rubio Bollinger, J. van Ruitenbeek, C. Urbina and E. Scheer, *Nature*, 1998, **394**, 154.
17 J. L. Costa-Krämer, N. García, P. García-Mochales and P. A. Serena, *Surf. Sci.*, 1995, **342**, L1144.
18 H. Ohnishi, Y. Kondo and K. Takayanagi, *Nature*, 1998, **395**, 780; A. I. Yanson, G. Rubio Bollinger, H. E. van den Brom, N. Agraït and J. M. van Ruitenbeek, *Nature*, 1998, **395**, 783.
19 Y. Kondo and K. Takayanagi, *Bull. Am. Phys. Soc.*, 1999, **44**, 312.
20 A. Torres, E. Tosatti, A. dal Corso, F. Ercolessi, J. J. Kohanoff, F. Di Tolla and J. M. Soler, *Surf. Sci. Lett.*, 1999, **426**, L441.
21 D. Sánchez-Portal, J. Junquera, P. Ordejón, A. García, E. Artacho and J. M. Soler, *Phys. Rev. Lett.*, 1999, **83**, 3884.
22 See, for instance: R. L. Whetten, J. T. Khoury, M. M. Alvarez, S. Murthy, I. Vezmar, Z. L. Wang, P. W. Stephens, C. L. Cleveland, W. D. Luedtke and U. Landman, *Adv. Mater.*, 1996, **5**, 8.
23 W. D. Luedtke and U. Landman, *J. Phys. Chem.*, 1996, **100**, 13323.
24 C. L. Cleveland, U. Landman, T. G. Schaaff, M. N. Shafigullin, P. W. Stephens and R. L. Whetten, *Phys. Rev. Lett.*, 1997, **79**, 1873.
25 J. A. Ascencio, C. Gutierrez-Wing, M. E. Espinosa, M. Marín, S. Tehuacanero, C. Zorrilla and M. J. Yacamán, *Surf. Sci.*, 1998, **396**, 349.
26 I. L. Garzón and A. Posada-Amarillas, *Phys. Rev. B*, 1996, **54**, 11796.
27 I. L. Garzón, K. Michaelian, M. R. Beltrán, A. Posada-Amarillas, P. Ordejón, E. Artacho, D. Sánchez-Portal and J. M. Soler, *Phys. Rev. Lett.*, 1998, **81**, 1600.
28 J. M. Soler, M. Beltrán, K. Michaelian, I. L. Garzón, P. Ordejón, D. Sánchez-Portal and E. Artacho, *Phys. Rev. B*, 2000, **61**, 5771.
29 K. Michaelian, *Chem. Phys. Lett.*, 1998, **293**, 202.
30 For recent reviews see: C. J. Kepert, M. Kurmoo and P. Day, *Proc. R. Soc. London, Ser. A*, 1998, **454**, 487; E. Coronado and C. Gómez-García, *Chem. Rev.*, 1998, **98**, 273.
31 A. Pénicaud, K. Boubekeur, P. Batail, E. Canadell, P. Auban-Senzier and D. Jérome, *J. Am. Chem. Soc.*, 1993, **115**, 4101.
32 S. Uriel, K. Boubekeur, P. Batail, J. Orduna and E. Canadell, *Inorg. Chem.*, 1995, **34**, 5307.
33 P. Batail, K. Boubekeur and A. Deluzet, unpublished results; C. Guilbaut, PhD Thèse, Université de Nantes, 1999; A. Deluzet, PhD Thèse, Université de Nantes, 2000.
34 P. Batail, K. Boubekeur, C. Guilbaud, A. Deluzet, C. Pasquier, P. Auban-Senzier, D. Jérome, R. Rousseau and E. Canadell, unpublished results.
35 M.-H. Whangbo, J. Ren, W. Liang, E. Canadell, J. P. Pouget, S. Ravy, J. M. Williams and M. A. Beno, *Inorg. Chem.*, 1992, **31**, 4169.
36 *Low-Dimensional Electronic Properties of Molybdenum Bronzes and Oxides*, ed. C. Schlenker, Kluwer, Dordrecht, 1989; *Physics and Chemistry of Low-Dimensional Inorganic Conductors*, ed. M. Greenblatt, C. Schlenker, J. Dumas and S. van Smaalen, *NATO ASI Ser., Ser. B*, Plenum, New York, 1996.
37 M. Greenblatt, *Chem. Rev.*, 1988, **88**, 31; C. Schlenker, J. Dumas, C. Escribe-Filippini, H. Guyot, J. Marcus and J. Fourcadot, *Philos. Mag. B*, 1985, **52**, 643.
38 J. Dumas and C. Schlenker, *Int. J. Mod. Phys. B*, 1993, **7**, 4045.
39 M. Greenblatt, *Int. J. Mod. Phys. B*, 1993, **7**, 3937.
40 P. Foury and J. P. Pouget, *Int. J. Mod. Phys. B*, 1993, **7**, 3973; A. Ottolenghi and J. P. Pouget, *J. Phys. I*, 1996, **6**, 1059.
41 C. Schlenker, C. Hess, C. Le Touze and J. Dumas, *J. Phys. I*, 1996, **6**, 2061; J. Dumas, C. Hess, C. Schlenker, G. Bonfait, E. Gomez Marín, D. Groult and J. Marcus, *Eur. Phys. J. B*, 2000, **8**, 9923.
42 E. Canadell and M.-H. Whangbo, *Phys. Rev. B*, 1991, **43**, 1894; E. Wang, M. Greenblatt, I. E.-I. Rachidi, E. Canadell, M.-H. Whangbo and S. Vadlamannati, *Phys. Rev. B*, 1989, **39**, 12969.
43 E. Canadell and M.-H. Whangbo, *Int. J. Mod. Phys. B*, 1993, **7**, 4005.
44 B. Raveau, *Proc. Indian Nat. Sci. Acad.*, 1986, **A52**, 67.
45 M.-H. Whangbo, E. Canadell, P. Foury and J. P. Pouget, *Science*, 1991, **252**, 96.
46 C. Schlenker, J. Dumas, C. Escribe-Filippini and H. Guyot, in

Low-Dimensional Electronic Properties of Molybdenum Bronzes and Oxides, ed. C. Schlenker, Kluwer, Dordrecht, 1989, p. 159.

47 M. Greenblatt, in *Low-Dimensional Electronic Properties of Molybdenum Bronzes and Oxides*, ed. C. Schlenker, Kluwer, Dordrecht, 1989, p. 1.

48 J. P. Pouget, in *Low-Dimensional Electronic Properties of Molybdenum Bronzes and Oxides*, ed. C. Schlenker, Kluwer, Dordrecht, 1989, p. 87.

49 H. Vincent, M. Ghedira, J. Marcus, J. Mercier and C. Schlenker, *J. Solid State Chem.*, 1987, **47**, 113.

50 M.-H. Whangbo, E. Canadell and C. Schlenker, *J. Am. Chem. Soc.*, 1987, **109**, 6308.

51 R. Moret and J. P. Pouget, in *Crystal Chemistry and Properties of Materials with Quasi-One-Dimensional Structures*, ed. J. Rouxel, Reidel, Dordrecht, 1986, p. 87.

52 K. Breuer, C. Stagarescu, K. E. Smith, M. Greenblatt and K. Ramanujachary, *Phys. Rev. Lett.*, 1996, **76**, 3172.

53 G.-H. Gweon, J. W. Allen, R. Claessen, J. A. Clack, D. M. Poirier, P. J. Benning, G. C. Olson, W. P. Ellis, Y.-X. Zhang, L. F. Schneemeyer, J. Marcus and C. Schlenker, *J. Phys.: Condens. Matter*, 1996, **8**, 9923.

54 M. Ghedira, H. Vincent, M. Marezio, J. Marcus and G. Fourcadot, *J. Solid State Chem.*, 1985, **56**, 66; L. Kihlborg, *Ark. Kemi*, 1963, **21**, 365; A. Magnéli, *Acta Chem. Scand.*, 1948, **2**, 861.

55 R. A. McKee, F. J. Walker and M. F. Chisholm, *Phys. Rev. Lett.*, 1998, **81**, 3014.

56 J. Wang, J. Hallmark, D. S. Marshall, W. J. Ooms, P. Ordejón, J. Junquera, D. Sánchez-Portal, E. Artacho and J. M. Soler, *Phys. Rev. B*, 1999, **60**, 4968.

57 C.-P. Cheng, I.-H. Hong and T.-W. Pi, *Phys. Rev. B*, 1998, **58**, 4066.

58 X. Yao, X. Hu, D. Sarid, Z. Yu, J. Wang, D. S. Marshall, R. Droopad, J. K. Abrokwah, J. A. Hallmark and W. J. Ooms, *Phys. Rev. B*, 1999, **59**, 5115.

59 G. Tobías and P. Ordejón, unpublished results.

60 J. I. Pascual, J. Gómez-Herrero, C. Rogero, A. M. Baró, D. Sánchez-Portal, E. Artacho, P. Ordejón and J. M. Soler, *Chem. Phys. Lett.*, 2000, **231**, 78.